

The $3d$ and $5d$ electronic structures and orbital hybridization in Ba- and Ca-doped $\text{La}_2\text{CoIrO}_6$ double perovskite

J. R. L. Mardegan,¹ L. S. I. Veiga,² T. Pohlmann,¹ S. S. Dhesi,² S. Francoual,¹ J. R. Jesus,³ C. Macchiutti,³ E. M. Bittar,³ and L. Bufaiçal^{4, *}

¹*Deutsches Elektronen-Synchrotron DESY, Notkestraße 85, 22607, Hamburg, Germany*

²*Diamond Light Source, Chilton, Didcot, Oxfordshire, OX11 0DE, United Kingdom*

³*Centro Brasileiro de Pesquisas Físicas, 22290-180, Rio de Janeiro, RJ, Brazil*

⁴*Instituto de Física, Universidade Federal de Goiás, 74001-970, Goiânia, GO, Brazil*

(Dated: June 21, 2023)

Here we present a detailed investigation of the Co and Ir local electronic structures in $\text{La}_{1.5}\text{A}_{0.5}\text{CoIrO}_6$ ($A = \text{Ba}, \text{Ca}$) compounds in order to unravel the orbital hybridization mechanism in these CoIr-based double perovskites. Our results of x-ray powder diffraction, ac and dc magnetization, Co and Ir $L_{2,3}$ -edges and Co K -edge x-ray absorption spectroscopy and x-ray magnetic circular dichroism suggest a competition between magnetic interactions. A dominant antiferromagnetic coupling is found to be responsible for the ferrimagnetic behavior observed for $A = \text{Ca}$ below ~ 96 K, the competing magnetic phases and the cationic disorder in this compound giving rise to a spin-glass state at low temperatures. For the $A = \text{Ba}$, on the other hand, there is no evidence of long range order down to its spin-glass transition temperature. The remarkably different magnetic properties observed between these two compounds is discussed in terms of the structural distortion that alters the strength of the Co – Ir couplings, with a relevant role played by the Co $3d e_g$ – Ir $5d j_{eff} = 1/2$ hybridization.

I. INTRODUCTION

Since the discovery of ferrimagnetism (FIM) and half-metallic behavior above room temperature (T) in $\text{Sr}_2\text{FeMoO}_6$ [1], double perovskites (DP) with various compositions have been produced and characterized in view of tuning the electronic and magnetic properties for spintronic applications. The most interesting properties are observed when the systems contain a combination of $3d$ and $4d/5d$ transition-metal (TM) ions [2, 3]. Ir-based DPs have recently received considerable attention due to the peculiar interplay between the strong spin-orbit coupling (SOC), the Coulomb repulsion, and the crystal field splitting which, in octahedral coordination, lifts the Ir t_{2g} orbital degeneracy into a fourfold $j_{eff} = 3/2$ and a $j_{eff} = 1/2$ doublet, giving rise to unusual magnetic properties [4, 5].

The use of Co as $3d$ TM in addition to $5d$ TM adds further complexity to the stabilization of magnetism in these Ir-based DPs. A delicate balance between crystal field and interatomic exchange interactions can lead to different valences and spin states of the Co ions in the octahedral symmetry [6]. In particular, $\text{La}_2\text{CoIrO}_6$ shows exciting properties such as magnetodielectric effect [7] and cooperative octahedral breathing distortion [8]. There is, however, some controversy concerning the microscopic mechanisms governing its magnetic properties.

N. Narayanan *et al.*, from the analysis of neutron powder diffraction (NPD) data, ascribed the small ferromagnetic (FM)-like behavior in $\text{La}_2\text{CoIrO}_6$ to spin canting in the two interpenetrating antiferromagnetic (AFM) Co

and Ir sublattices [9]. However, the strong neutron absorption of Ir ions prevents a reliable determination of its magnetic structure. On the other hand, recent studies using x-ray absorption spectroscopy (XAS), x-ray magnetic circular dichroism (XMCD), and muon spin spectroscopy suggest an AFM coupling between Co and Ir FM sublattices, resulting in a ferrimagnetic (FIM) behavior [10, 11]. The small magnetization observed in the system can be ascribed to the antisite disorder (ASD) at Co/Ir sites and the competing magnetic interactions that lead to frustration. There are also other interpretations. Min-Cheol Lee *et al.*, using Co and O K -edge XAS, claim that the spin frustration and extended paramagnetic (PM) phase are due to the non spin-selective nature of the Co^{2+} ($3d e_g \oplus 4p$) – Ir^{4+} $5d e_g$ coupling [12]. At the same time, recent Ir L_3 -edge resonant inelastic x-ray scattering show the importance of the $3d$ - $5d$ hybridization in the magnetism of Ir-based DPs [13]. Additionally, x-ray photoelectron spectroscopy measurements point to a large covalence in several DP iridates, questioning the description of these materials by a simple ionic picture [14].

The observations reported above indicate how far we are from reaching a consensus on the nature of the magnetic ordering in Ir-based DPs. This is also valid when La is partially replaced by alkaline-earth in $\text{La}_2\text{CoIrO}_6$. For $\text{La}_{2-x}\text{Sr}_x\text{CoIrO}_6$, a structural transition accompanied by changes in the Co/Ir valences and magnetic structures is observed even for small Sr-doping [9, 15]. For $\text{La}_{2-x}\text{Ca}_x\text{CoIrO}_6$, on the other hand, there is no structural transition, and up to 25% of Ca to La, the substitution acts mainly at changing the Co valence, with Ir remaining nearly tetravalent [11]. The $x = 0.5$ concentration is of particular interest due to its compensation temperatures and spontaneous exchange bias effect [16],

* lbufaical@ufg.br

which seems to be directly related to a re-entrant spin glass (RSG) phase [17, 18]. Likewise, the Sr to La partial substitution also induces competition between magnetic phases that leads to RSG [19], whereas the $\text{La}_2\text{CoIrO}_6$ parent compound does not show glassy magnetic behavior.

In order to shed light on the role of the Co $3d$ – Ir $5d$ orbital hybridization in stabilizing the magnetic coupling in CoIr-based DPs, we have performed a detailed investigation of how the crystal structure affects the electronic and magnetic structures of Co and Ir sublattices in $\text{La}_{1.5}(\text{Ba,Ca})_{0.5}\text{CoIrO}_6$ compounds using x-ray powder diffraction (XRD), ac and dc magnetization, XAS and XMCD. Our results show remarkably different magnetic properties for these compounds, that are discussed in terms of the lattice distortions which ones alter the orbital hybridization between Co and Ir.

II. EXPERIMENTAL DETAILS

The polycrystalline samples here investigated were synthesized by conventional solid-state reaction. To obtain $\text{La}_{1.5}\text{Ba}_{0.5}\text{CoIrO}_6$ (hereafter called Ba0.5), stoichiometric amounts of La_2O_3 , BaCO_3 , Co_3O_4 and metallic Ir in powder form were mixed and heated at 650°C for 24 hours in air atmosphere. Later, the sample was re-grounded before a second step at 800°C for 48 hours. Finally, the material was grinded, pressed into a pellet, and heated at 1200°C for additional 48 hours. The synthesis route used to produce $\text{La}_{1.5}\text{Ca}_{0.5}\text{CoIrO}_6$ (herein called Ca0.5) is described elsewhere [11].

High-resolution XRD data were collected at room temperature using a Cu K_α radiation operating at 40 kV and 40 mA at Centro Brasileiro de Pesquisas Físicas (CBPF), Brazil. The XRD data was carried over the angular range of $10^\circ \leq 2\theta \leq 110^\circ$, with a 2θ step size of 0.01° . Rietveld refinement was performed using GSAS software and its graphical interface program [20]. The ac and dc magnetic measurements were carried out using a Quantum Design PPMS magnetometer, at CBPF.

Low-temperature XAS measurements were carried out at the Co K - and Ir $L_{2,3}$ -absorption edges on beamline P09 at PETRA III at the DESY [21] and at Co $L_{2,3}$ -absorption edges on beamline I06 at Diamond Light Source (DLS). For the hard x-ray measurements, fine powder samples were mixed and pressed into a low-Z BN material to produce pellets for transmission measurements. XMCD measurements were performed at 5 K by fast-switching the beam helicity between left and right circular polarization [22]. In order to align the magnetic domains and correct for nonmagnetic artifacts, an external magnetic field of ± 5 T was applied parallel and antiparallel to the incident beam wave vector k using a 6T/2T/2T vector magnet. For the soft x-ray measurements, powder samples from the same batches were spaded on conductive carbon tapes and measured in total electron yield (TEY). The samples were cooled at 2

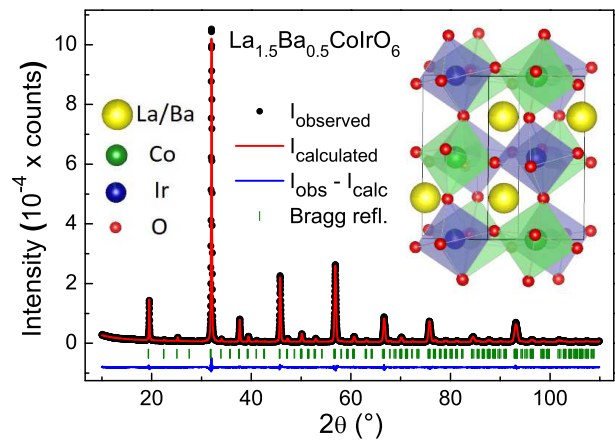


FIG. 1. Rietveld refinement fitting of Ba0.5 XRD. The vertical lines represent the Bragg reflections for the $P2_1/n$ space group. Inset shows the crystal structure, in which IrO_6 and CoO_6 are drawn as blue and green octahedra, respectively.

K, and an external magnetic field of ± 5 T was applied along the beam axis to reach saturation.

III. RESULTS AND DISCUSSION

A. x-ray diffraction

Fig. 1 shows the XRD pattern of Ba0.5, which confirms the formation of a perovskite structure with no trace of impurity phase. Previous studies on $\text{La}_2\text{CoIrO}_6$ and LaBaCoIrO_6 show that the former compound grows in the monoclinic $P2_1/n$ space group whereas the latter was reported as belonging to the triclinic $\bar{1}$ non-standard space group [9, 11, 23]. Such non-standard setting is commonly adopted to facilitate the comparison of this structure with that of other DPs [3, 24]. In our case, a detailed investigation of the XRD data of the Ba0.5 sample revealed that some of the experimentally observed reflections are not predicted for the triclinic symmetry. In contrast, all peaks match with that of the monoclinic structure. Therefore, the 25% of Ba substitution at the La site is not sufficient to induce a structural transition, with Ba0.5 belonging to the $P2_1/n$ space group, the same as that of Ca0.5 [11]. The main results obtained from the Rietveld refinement are displayed in Table I, where the structural parameters of Ca0.5 (some of them already reported in Ref. 11) are also shown for comparison.

From Table I we observe an increase in the unit cell volume (V) of Ba0.5 as compared to Ca0.5, in agreement with the Ba^{2+} ionic radius being larger than Ca^{2+} (respectively 1.61 and 1.34 Å in XII coordination [25]). Interestingly, although both compounds belong to the $P2_1/n$ monoclinic space group, there is a tendency towards a more tetragonal symmetry for Ba0.5, which is manifested by the closeness of the a and b lattice pa-

rameters and a significant increase in the c parameter. The increased crystallographic symmetry is expected for larger rare-earth/alkaline-earth ionic radii in DPs [2, 3], manifested in the increased Co–O–Ir bond angles and the more similar Co–O and Ir–O bond lengths for Ba0.5. It must also be noticed in Table I that the Co/Ir ASD, *i.e.* the amount of Co(Ir) ions lying at Ir(Co) site, is rather similar for both compounds. Though this may look unexpected at a first glance, since an increased crystallographic symmetry usually leads to larger ASD, we recall that Ca0.5 was synthesized at 1000°C [11] while Ba0.5 was produced at 1200°C. The synthesis condition was already shown to play a role on the B/B' cationic ordering of DPs, which commonly increases with increasing the synthesis temperature [26].

B. ac and dc magnetization

Fig. 2(a) shows the zero-field cooled (ZFC) and field cooled (FC) dc magnetic susceptibility (χ_{dc}) data for Ba0.5, measured with a magnetic field (H) of 0.05 T. For comparison, Fig. 2(b) displays χ_{dc} curves for Ca0.5 also measured with $H = 0.05$ T, as reported in Ref. 11. For Ca0.5, the higher- T FM-like magnetic transition at $T \sim 96$ K is ascribed to Co²⁺–O–Ir⁴⁺ AFM coupling that results in FIM. At the same time, the peak at $T \sim 27$ K is related to the emergence of a spin glass (SG) phase caused by competing magnetic interactions and ASD [11].

For Ba0.5, although there is only one clear peak at $T \sim 24$ K in the χ_{dc} data, a bifurcation of the ZFC and FC curves at $T \sim 85$ K is observed, at which temperature a deviation of the Curie-Weiss law is also observed in the inverse susceptibility [inset of Fig. 2(a)]. This could indicate that a non-percolating short-range magnetic coupling starts to develop around this temperature, which could be in turn related to the appearance of a spin-glass phase at much lower temperatures. The emergence of short-range correlations and fluctuations far above the freezing temperature is commonly observed in spin-glasses [27].

The real part of the ac magnetic susceptibility (χ'_{ac}) curves measured for Ba0.5 in an oscillating field $H_{ac} = 10$ Oe with six ac frequencies (f) ranging from 30 to 10000 Hz is shown on Fig. 2(c). In contrast to the ac magnetic susceptibility data for Ca0.5, where a clear cusp is observed at T_C [inset of Fig. 2(d)], the χ'_{ac} curves of Ba0.5 gives no evidence of any anomaly close to 85 K, further indicating that the weak magnetic coupling between Co and Ir does not percolate on this compound. At lower temperatures, it is observed a systematic decrease in the amplitude of the $T \sim 24$ K peak and its shift to higher temperatures as f increases. These are characteristic features of glassy magnetism, signaling that this peak corresponds to the freezing temperature (T_f) of a SG-like phase [28]. The evolution of T_f with f turns out to be well fitted by the power-law equation of the dynamic scaling theory, commonly used to investigate

SG-like systems

$$\frac{\tau}{\tau_0} = \left[\frac{(T_f - T_g)}{T_g} \right]^{-z\nu}, \quad (1)$$

where τ is the relaxation time corresponding to the measured frequency, τ_0 is the characteristic relaxation time of spin flip, T_g is the SG transition temperature (T_f as f tends to zero), z is the dynamical critical exponent and ν is the critical exponent of the correlation length [28, 29]. The solid line on inset of Fig. 2(c) represents the fit to Eq. 1, yielding $T_g \simeq 24.4$ K, $\tau_0 \simeq 6.3 \times 10^{-12}$ s and $z\nu \simeq 5.9$, being these values typical of conventional SG systems [16, 29, 30].

Usually, the relative shift $\delta T_f = \Delta T_f / T_f (\Delta \ln f)$ is calculated to classify the material as canonical SG, cluster SG or superparamagnet. For Ba0.5 we find $\delta T_f \simeq 0.006$, which is within the range usually found for canonical SG ($\delta T_f < 0.01$ [30–32]). This confirms that, as for Ca0.5, the ASD and competing magnetic interactions also lead to the emergence of a SG phase in Ba0.5.

The fit of the PM region of $1/\chi_{dc}$ raw data with the Curie-Weiss (CW) law, inset of Fig. 2(a), yields a CW temperature $\theta_{CW} = -58$ K for Ba0.5. The negative sign indicates that AFM couplings dominate the magnetic interactions in this compound, as observed for Ca0.5 [11]. The $\mu_{eff} = 5.3 \mu_B/\text{f.u.}$ obtained from the fit is fairly close to the value found for Ca0.5 ($5.4 \mu_B/\text{f.u.}$) [11]. It is important to mention that the situation here is quite different from that of some Ir⁵⁺-based compounds where a χ_0 term is usually included in the CW equation to account for a diamagnetic contribution to the susceptibility [5, 33–35]. In our Ir⁴⁺/Co^{2+,3+} system, the van-Vleck constant term and the core diamagnetic contribution are expected to be negligible regarding the paramagnetic moments of the TM ions.

Fig. 2(d) displays the magnetization as a function of H [M(H)] curves measured at 5 K for Ba0.5 and Ca0.5 samples. Both curves are typical of FIM systems, with a FM-like hysteresis but a linear increase of magnetization at high H , further indicating the presence of AFM interactions. It is interesting to notice the remarkable decrease in the coercive field (H_C) of Ba0.5 with respect to Ca0.5. This resembles other 3d-5d DPs for which H_C dramatically decreases with the expansion of the unit cell [36–39].

C. XAS and XMCD measurements

XAS spectra at the TM $L_{2,3}$ -edges are very sensitive to the valence state, corresponding to electronic transitions from the $2p$ to $3d$ ($5d$) orbitals for ions of the first (third) row. Fig. 3(a) shows the Co $L_{2,3}$ -edge spectra for the samples of interest together with those of CoO and LaCoO₃, used here as standards for Co²⁺ and Co³⁺, respectively. The presence of Co²⁺ in Ba0.5 and Ca0.5 samples is confirmed by the similarity of the spectra with

TABLE I. Main results obtained from the Rietveld refinements of the room temperature XRD data. Some of the parameters displayed for Ca0.5 were already reported in Ref. 11.

Lattice Parameters and R factors												
Sample	a (Å)	b (Å)	c (Å)	β (°)	V (Å ³)	R_p (%)	R_{wp} (%)					
Ca0.5	5.5566(1)	5.6427(2)	7.8808(2)	89.98(1)	247.09(2)	8.5	11.2					
Ba0.5	5.6326(2)	5.6152(1)	7.9402(3)	90.02(1)	251.13(1)	4.0	5.6					
Bonds and Angles												
Sample	Co-O ₁ (Å)	Co-O ₂ (Å)	Co-O ₃ (Å)	(Co-O) (Å)	Ir-O ₁ (Å)	Ir-O ₂ (Å)	Ir-O ₃ (Å)	(Ir-O) (Å)	Co-O ₁ -Ir (°)	Co-O ₂ -Ir (°)	Co-O ₃ -Ir (°)	(Co-O-Ir) (°)
Ca0.5	2.062(13)	2.127(13)	2.072(15)	2.087(8)	1.980(13)	2.033(13)	2.076(15)	2.030(8)	156.7(8)	144.4(7)	143.6(5)	148.2(4)
Ba0.5	2.023(1)	2.060(1)	1.996(1)	2.023(1)	2.012(1)	2.043(1)	2.071(1)	2.042(1)	162.2(1)	151.4(1)	154.8(1)	156.1(1)
Atomic Coordinates and Thermal Displacement Parameters												
Sample	atom	Wyckoff position	occupancy	x	y	z	U_{iso} (Å ²)					
Ca0.5	La/Ca	4e	0.75/0.25	0.5103(3)	0.5437(5)	0.2503(3)	0.0105(5)					
	Co1/Ir1	2c	0.927/0.073(3)	0	0.5	0	0.0121(3)					
	Ir2/Co2	2d	0.927/0.073(3)	0.5	0	0	0.0121(3)					
	O1	4e	1	0.2188(21)	0.2093(23)	0.9629(27)	0.0045(24)					
	O2	4e	1	0.3064(21)	0.7076(24)	0.9363(23)	0.0045(24)					
	O3	4e	1	0.3842(22)	0.9867(18)	0.2503(20)	0.0045(24)					
Ba0.5	La/Ba	4e	0.75/0.25	0.5140(2)	0.5271(1)	0.2474(5)	0.0104(2)					
	Co1/Ir1	2c	0.936/0.064(2)	0	0.5	0	0.0129(2)					
	Ir2/Co2	2d	0.936/0.064(2)	0.5	0	0	0.0129(2)					
	O1	4e	1	0.2475(26)	0.2474(25)	0.9608(29)	0.0072(12)					
	O2	4e	1	0.3039(30)	0.6980(31)	0.9645(23)	0.0072(12)					
	O3	4e	1	0.4214(28)	0.9996(11)	0.2548(29)	0.0072(12)					

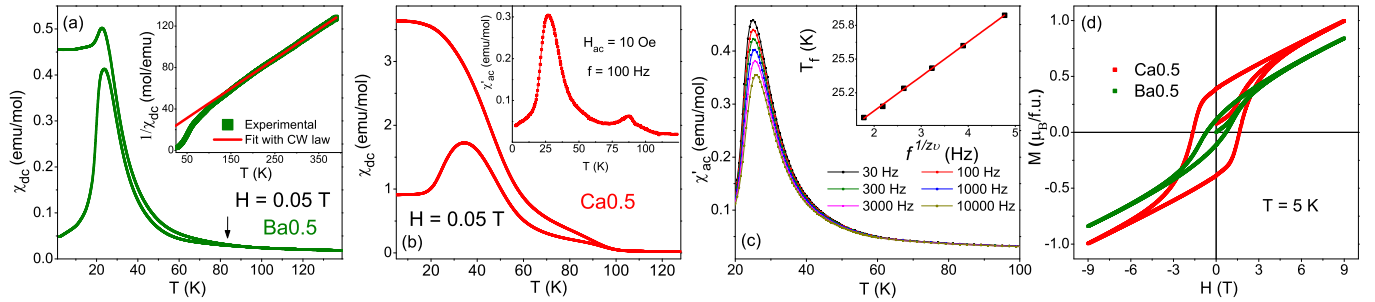


FIG. 2. (a) ZFC-FC χ_{dc} curves for Ba0.5, measured with $H = 0.05$ T. The arrow indicates the temperature where the curves bifurcate, and the inset shows the best fit of PM region with the CW law. (b) ZFC-FC χ_{dc} curves measured with $H = 0.05$ T for Ca0.5, adapted from Ref. 11. Inset shows the χ_{ac} curve measured with $H_{ac} = 10$ Oe, $f = 100$ Hz. (c) χ'_{ac} as a function of T for Ba0.5 at different f , measured with $H_{ac} = 10$ Oe. Inset shows T_f as a function of f , where the solid line represents the best fit to the data using Eq. 1. (d) $M(H)$ curves for Ba0.5 and Ca0.5 samples, measured at 5 K.

that of CoO. However, for Ba0.5 it is observed the presence of pronounced peaks at ~ 785 and ~ 800 eV, associated with Ba $M_{4,5}$ absorption edges. A closer inspection of the higher energy side of the L_3 -edge (~ 780 eV) of Ca0.5 and Ba0.5 reveals a relative increase in the intensity of the spectra with respect to that of CoO near the energy position of Co^{3+} L_3 -edge absorption, suggesting that some fraction of Co is in trivalent state. This is in agreement with the effective magnetic moments obtained for both compounds [11].

A quantitative estimate of the Co oxidation state can be made for our Ca0.5 sample by comparing the *center of mass* of its L_3 -edge spectrum with those of the reference samples. Assuming a linear variation in energy between the *center of mass* of Co^{2+} and Co^{3+} , the Co formal valence was estimated to be ~ 2.4 for Ca0.5, which would mean the presence of $\sim 10\%$ of Ir^{5+} or oxygen vacancy in this sample. Surely this is just a rough estimate, since other parameters such as the crystal field and structure may play a role on the integrated intensity of XAS curves. Nevertheless, a $+2.4$ formal valence is reasonably close to the $+2.5$ value expected for a 25% Ca^{2+} to La^{3+} substitution, which one would act mainly at changing the Co

valence, a scenario corroborated by the magnetometry results and Ir L_3 -edge XAS. For Ba0.5, the presence of the Ba- M_5 absorption peak nearby the Co L_3 -edge curve affects the calculation of the *center of mass*, preventing a reliable estimate of its valence state. Notwithstanding, the similarity of its $L_{2,3}$ -edge curves with that of Ca0.5, as well as the closeness of the μ_{eff} observed for both samples, suggest that the Co valence for Ba0.5 is similar to that of Ca0.5.

Figs. 3(b) and (c) show the Co $L_{2,3}$ XMCD of Ca0.5 and Ba0.5 samples, respectively. The same overall behavior suggests nearly the same magnetic structure for both compounds. The black and red curves stand respectively for μ^+ and μ^- , *i.e.*, for parallel and antiparallel alignments between the photon spin and H , and the difference spectra $\Delta\mu = \mu^+ - \mu^-$ corresponds to the blue line. As can be noticed, the XMCD signal is largely negative at L_3 -edge but with a very small positive value at L_2 -edge, indicating non-negligible orbital contribution to the magnetic moment, as commonly observed for Co in octahedral coordination [6]. For a quantitative analysis of the Co- $L_{2,3}$ XMCD spectra, we have used the sum rules to derive the orbital and spin contributions to the

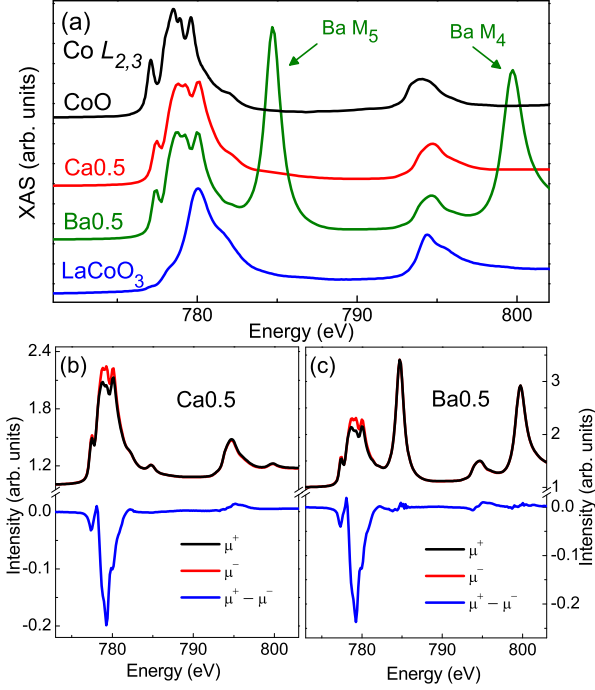


FIG. 3. (a) Co $L_{2,3}$ -edge XAS spectra of Ca0.5 and Ba0.5 samples, together with those of CoO (reference for Co^{2+}) and LaCoO_3 (reference for Co^{3+}). The presence of Ba $M_{4,5}$ -edges in Ba0.5 sample is highlighted by green arrows. (b) and (c) show respectively the XMCD spectra of Ca0.5 and Ba0.5 samples, taken at 2 K with $H = 5$ T. The photon spin was aligned parallel (μ^+ , black) and antiparallel (μ^- , red) to H , and the difference spectra are shown in blue.

magnetization [41, 42]

$$m_l = -\frac{4 \int_{L_3+L_2} (\mu^+ - \mu^-) d\omega}{3 \int_{L_3+L_2} (\mu^+ + \mu^-) d\omega} N_h, \quad (2)$$

$$m_s = -\frac{6 \int_{L_3} (\mu^+ - \mu^-) d\omega - 4 \int_{L_3+L_2} (\mu^+ - \mu^-) d\omega}{\int_{L_3+L_2} (\mu^+ + \mu^-) d\omega} \times N_h \left(1 + \frac{7 \langle T_z \rangle}{2 \langle S_z \rangle} \right)^{-1}, \quad (3)$$

where m_l and m_s are the angular and spin magnetic moments in units of μ_B/atom , S_z denotes the projection along z of the spin magnetic momentum, N_h represent the number of empty $3d$ states, T_z denotes the magnetic dipole moment, and L_2 and L_3 represent the integration

range. Here we used $N_h = 3.5 \pm 0.5$, which is an approximated atomistic value corresponding to a mixture of Co^{2+} ($N_h = 3$) and Co^{3+} ($N_h = 4$). Moreover, T_z is estimated to be negligible against S_z for TM ions in octahedral symmetry [43, 44]. With these considerations, we obtained $m_l = 0.15 \mu_B$ and $m_s = 0.29 \mu_B$. Considering sources of deviations such as electronic interactions, imprecision in the integral calculations, and the N_h value assumed, we estimate an uncertainty of $\sim 20\%$ on these values [43, 44].

The calculated moments are similar to those reported for $\text{La}_2\text{CoIrO}_6$ ($m_l = 0.18 \mu_B$, $m_s = 0.31 \mu_B$) [10], which is somewhat unexpected considering that from our XAS spectra we can expect about 40% of the Co ions in a trivalent state, as opposed to a presumably 100% of Co^{2+} in $\text{La}_2\text{CoIrO}_6$. However, in Ref. 10 a quantitative investigation of the Co formal valence was not performed for the parent compound, whilst another study performed on a $\text{La}_2\text{CoIrO}_6$ polycrystalline sample produced by a similar synthesis route reported the presence of some amount of Co^{3+} [11]. Furthermore, the previous XMCD study reported for $\text{La}_2\text{CoIrO}_6$ in Ref. 10 was carried out at 43 K using $H = 0.8$ T, while element-specific hysteresis curves measured for CoIr-DPs have already shown that Co is far from saturation at these conditions [15].

For the Ba0.5 sample, one must recall the pronounced Ba $M_{4,5}$ -edge peaks observed near the Co $L_{2,3}$ absorption edge. Although one may not expect a XMCD signal at the Ba $M_{4,5}$ -edge, the large XAS white line intensity may influence the background of the Co $L_{2,3}$ pre- and post-edge regions, and affect the adjustment of the XAS curve for the calculation of the $L_2 + L_3$ integral. Therefore, m_l and m_s were not estimated for this compound. The m_l/m_s ratio, however, is independent of the XAS integrated intensity, resulting in a trustworthy value that is fairly close to that found for Ca0.5.

In order to avoid the problem of Ba $M_{4,5}$ -edges, we investigated the Co K -edge XAS and XMCD, as shown in Fig. 4. The Co K -edge XAS reflects mainly the electric dipole transitions from $1s$ to $4p$ level, where the edge position in energy may probe the Co valence. At the same time, local arrangements of neighboring ions determine the region after the absorption threshold. The similarity between the curves displayed in Fig. 4(a) is in accordance with the same monoclinic structure and similar Co valence states for both compounds.

The inset of Fig. 4(a) shows a magnified view of the pre-edge region. Although the K -edge XAS reflects mostly the transitions to unoccupied Co $4p$ states, M.-C. Lee *et al.* showed that the pre-edge anomalies α and β_1 are related to Co $4p$ partial electron filling via intra-site mixing with Co $3d$ orbitals [12]. Thus, the orbital hybridization with Ir $5d$ orbitals may largely contribute to these pre-edge features (see Fig. 6). Interestingly, a third anomaly, $\beta_2 \sim 7720$ eV, is observed for Ca0.5 and Ba0.5, which may be related to Co^{3+} ($3d e_g \oplus 4p$) - Ir $5d e_g$ hybridization via O $2p$.

The Co K -edge XMCD signals measured at $T = 5$ K

TABLE II. Co and Ir orbital (m_l), spin (m_s) and total (m_t) magnetic moments obtained from the sum rules calculations of Co and Ir $L_{3,2}$ XMCD spectra.

Sample	Co m_l (μ_B)	Co m_s (μ_B)	Co m_t (μ_B)	Co m_l/m_s	Ir m_l (μ_B)	Ir m_s (μ_B)	Ir m_t (μ_B)	Ir m_l/m_s
Ca0.5	0.15 ± 0.03	0.29 ± 0.06	0.44 ± 0.07	0.52 ± 0.11	-0.11 ± 0.02	-0.11 ± 0.02	-0.22 ± 0.03	1.00 ± 0.21
Ba0.5	-	-	-	0.54 ± 0.15	-0.07 ± 0.01	-0.06 ± 0.01	-0.13 ± 0.01	1.17 ± 0.27

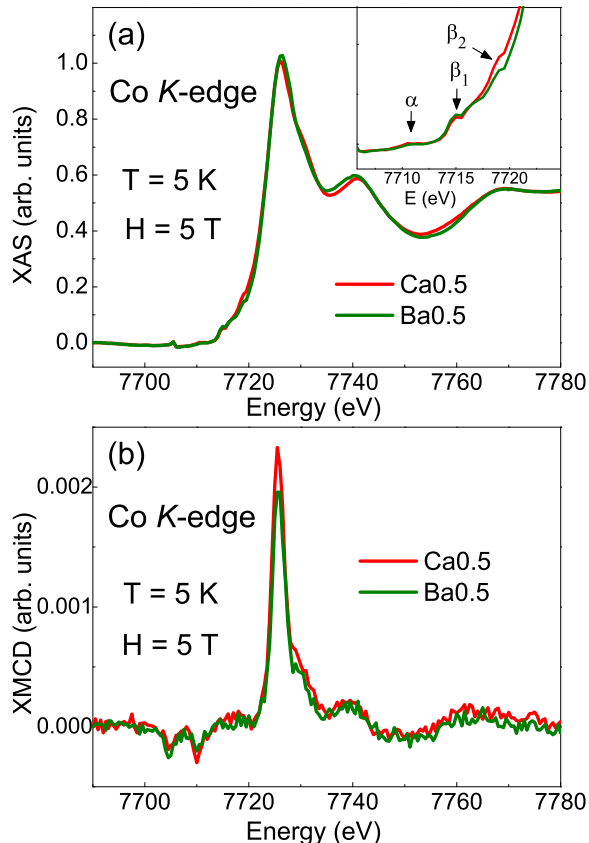


FIG. 4. (a) Co K -edge XAS spectra of Ba0.5 and Ca0.5 samples, measured at 5 K. Inset shows a magnified view of the pre-edge region, highlighting the α , β_1 and β_2 peaks. (b) The XMCD spectra of these samples.

and $H = 5$ T are very similar for both Ca0.5 and Ba0.5 [Fig. 4(b)], suggesting that although the Co $3d$ bands present a relative extended character, the changes in the crystallographic environment does not drastically affect the Co magnetism.

Similar scenario cannot be extrapolated to the Ir ions, since the $5d$ orbitals are even more extended than the Co $3d$, which makes Ir ions more sensitive to structural and electronic changes. Fig. 5(a) shows the Ir $L_{2,3}$ -edge XAS spectra of Ba0.5 and Ca0.5 samples together with that of IrO_2 , reference for Ir^{4+} state. The spectra of Ba0.5 and Ca0.5 are reasonably similar to that of IrO_2 , indicating that the majority of Ir ions are in a tetravalent state for both compounds. Nonetheless, the similarity between the curves is characteristic of the $L_{2,3}$ -edge spectra of

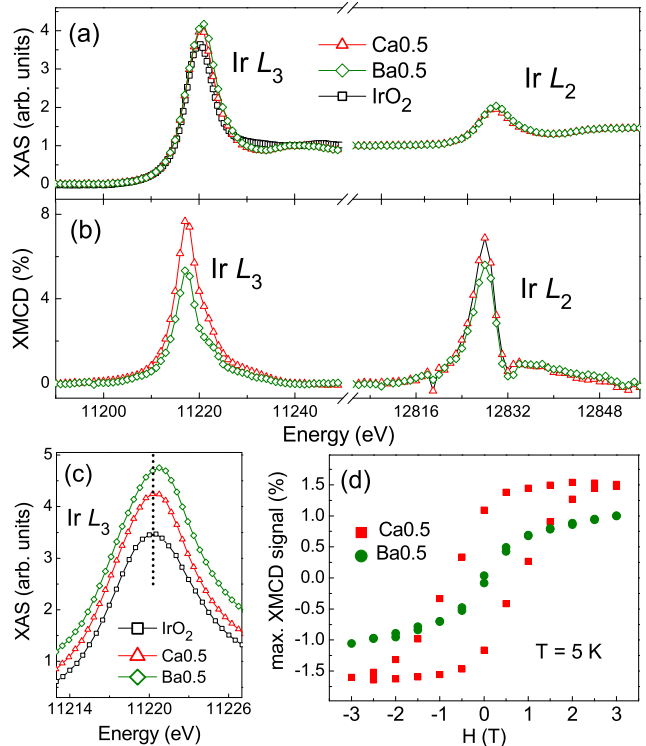


FIG. 5. Ir $L_{2,3}$ -edges: (a) XAS and (b) XMCD spectra for Ba0.5 and Ca0.5 measured at 5 K and under 5 T. (c) Magnified view of the L_3 -edge, where the IrO_2 standard is added for comparison. (d) Element-specific XMCD hysteresis loops of Ir L_3 -edge.

$5d$ TM ions, being related to the more diffuse valence orbitals compared to the $3d$ ones [15, 45]. A magnified view of the L_3 -edge region depicted in Fig. 5(c) indicates some subtle differences between the spectra. The Ca0.5 and Ba0.5 spectra are shifted of respectively ~ 0.2 eV and ~ 0.3 eV with respect to the IrO_2 L_3 XAS, suggesting the presence of a small amount of Ir^{5+} . However, these shifts lie within the instrumental resolution (~ 1.5 eV), while the difference in energy between the white line positions of Ir^{4+} and Ir^{5+} is of about 1.2 eV [34]. With

these considerations, we can only conclude that Ba0.5 and Ca0.5 presents nearly the same Ir valence state, with the majority of ions in a tetravalent state.

Fig. 5(b) shows the Ir $L_{2,3}$ -edge XMCD spectra measured at $T = 5$ K and $H = 5$ T. The positive signs of the Ir XMCD signals, combined with the negative sign for the Co signal, indicate that those two ions develop an AFM coupling in both compounds. Table II shows the Ir orbital and spin moments obtained from the sum rules, for which it was assumed $N_h = 5 \pm 0.5$ (Ir^{4+}). The m_l and m_s values found are similar to those previously reported for $\text{La}_{1.5}\text{Sr}_{0.5}\text{CoIrO}_6$ [15], and the large m_l/m_s ratio observed is typical of iridates and other $5d$ -based materials presenting strong SOC [46, 47]. The somewhat smaller moments observed for Ba0.5 with respect to Ca0.5 helps to explain its slightly smaller μ_{eff} obtained from the χ_{dc} curves, also suggesting that the Ir magnetization is closely related to its orbital hybridization with neighboring Co ions.

Fig. 5(c) shows element-specific hysteresis loops obtained by monitoring the Ir L_3 -edge XMCD signal as a function of H . As can be noticed, the Ir moment is nearly saturated for Ca0.5 under $H = 3$ T, whereas for Ba0.5 the saturation might be reached only for much higher magnetic fields. A remarkable point in these curves is the pronounced decrease in the H_C of Ba0.5 with respect to Ca0.5, as also observed in the macroscopic $M(H)$ curves measured in PPMS [Fig. 2(d)].

D. Discussion

In general, the magnetic ordering of TM ions in DPs can be described by the orbital hybridization mechanism, according to which the d orbital states reside close to the Fermi surface, being respectively slightly below the chemical potential for one TM ion and slightly above for another. Then, a hybridization between these orbitals, mediated by O $2p$ orbitals, enables the virtual spin-dependent electron hopping from one TM to another and can stabilize either FM or AFM coupling [2, 3]. For HS Co^{2+} (Co^{3+}), there are two (one) completely filled and one (two) half filled t_{2g} orbital(s), while both e_g orbitals are partially filled. The $5d^5$ Ir^{4+} ion, on the other hand, is at LS configuration, with the SOC lifting the t_{2g} degeneracy to a fourfold $j_{eff} = 3/2$ and a twofold $j_{eff} = 1/2$ state. Thus, Ir^{4+} has one $j_{eff} = 1/2$ electron while its $j_{eff} = 3/2$ orbitals are fully occupied [4, 48].

Recent first-principles calculations for $\text{La}_2\text{CoIrO}_6$ have shown that the energy of the Ir- $j_{eff} = 1/2$ state resides in between those of Co t_{2g} and e_g , whereas the strong crystal field splitting on Ir puts its e_g states ~ 3 eV higher in energy, making these later orbitals irrelevant to our discussion [49]. As a consequence, only the $t_{2g} - \text{O } 2p - t_{2g}$ π bonding would be a relevant exchange path between Co and Ir. However, although the $t_{2g} - \text{O } 2p - e_g$ coupling is in principle forbidden by symmetry in a cubic perovskite (*i.e.* for a 180° B-O-B' bond angle), it can

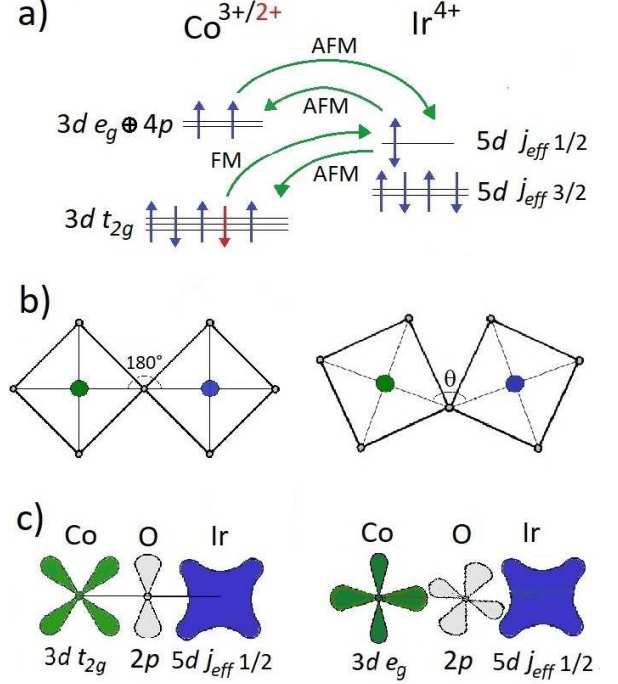


FIG. 6. (a) Schematic diagram of the mechanisms of hybridization between $\text{Co}^{2+/3+}$ ($3d^7/3d^6$) and Ir^{4+} ($5d^5$), where the red arrow represents an additional spin down electron for Co^{2+} t_{2g} , which is absent for Co^{3+} . The green arrows represent virtual electron hopping. The blue double-arrow in Ir $j_{eff} = 1/2$ is spin down for the case of AFM interaction and spin up for the FM case. (b) $(\text{Co}/\text{Ir})\text{O}_6$ octahedra geometries for Co-O-Ir bond angle $\theta = 180^\circ$ and $\theta < 180^\circ$. (c) The Co $t_{2g} - \text{Ir } j_{eff} = 1/2$ (left) and Co ($3d e_g + 4p$) - Ir $j_{eff} = 1/2$ (right) orbital hybridizations.

become possible with lattice distortion, as is the case for the samples here investigated.

Fig. 6(a) depicts the spin-selective exchange pathways between $\text{Co}^{2+}/\text{Co}^{3+}$ and Ir^{4+} in our system. There is one possible FM virtual hopping from the Co t_{2g} minority spin state to Ir t_{2g} ($j_{eff} = 1/2$), and a number of possible AFM couplings. Here we must recall the highly covalent character of the Ir-O bond, with an O-electron partially occupying the Ir- t_{2g} orbital [14], which in principle inhibits the virtual electron transfer from Co to Ir. This partial population of Ir- $j_{eff} = 1/2$ orbital with O-electrons, together with the SOC, may explain the dramatic decrease of the Ir magnetic moment observed here and for other Ir^{4+} -based perovskites [8, 9, 11, 15]. There-

fore, AFM charge transfer from Ir to Co seems to dominate the orbital hybridization in these samples, which is supported by the fact that all experimental and theoretical works reported so far for CoIr-based DPs points towards AFM coupling between these ions. As Fig. 6(a) shows, the intermediate charge transfer from Ir t_{2g} can occur to a Co t_{2g} or e_g orbital. A transfer to Co t_{2g} , through the Ir $t_{2g} - O 2p - Co t_{2g}$ pathway, is expected to be stronger for Ba0.5 than for Ca0.5, since the former compound presents increased Co–O–Ir bond angles [see Figs. 6(b) and (c)]. The fact that Ca0.5 shows a clear magnetic ordering at a relatively high temperature, contrasting the results found for Ba0.5, suggests that the Ir $t_{2g} - O 2p - Co t_{2g}$ is not the most relevant hybridization channel in these compounds. On the other hand, the Ir $t_{2g} - O 2p - Co e_g$ channel is expected to strengthen as the Co–O–Ir angle decreases, subsequently becoming the most relevant hybridization pathway between Co and Ir. This is reminiscent of other $3d-5d$ DPs, for which a systematic increase of the magnetic ordering temperature is observed as the B–O–B' angle decreases [36, 38, 39, 50]. The absence of a clear magnetic ordering for Ba0.5 is thus likely related to the weakened Ir $t_{2g} - O 2p - Co e_g$ and strengthened Ir $t_{2g} - O 2p - Co t_{2g}$ hybridization, with the competing magnetic interactions leading to spin frustration.

Another striking difference between Ba0.5 and Ca0.5 resides in their H_C . In other $3d-5d$ DPs, as well, changes in the orbital hybridization caused by structural distortions remarkably alter their magnetic properties. For $AA'FeReO_6$ ($AA' = Ba, Ca, Sr$), the increase of H_C and T_C was observed with decreasing the average A radius, which was ascribed to the increase of Re orbital moment due to lattice distortion [36]. Contrastingly, high-pressure studies in A_2FeReO_6 ($A = Ba, Ca$) showed a remarkable increase of H_C with increasing pressure that was not related to the increase of Re orbital contribution. Instead, such changes in H_C were explained in terms of reducing the strength of SOC caused by the structural distortion [37].

For our CoIr-based samples, the dramatic increase in the H_C of Ca0.5 with respect to Ba0.5 is probably not related to increase of the orbital moments since the Ir m_l value obtained for Ca0.5 is only slightly larger than that of Ba0.5, while the Co m_l/m_s ratio is higher for the latter compound. Here we must recall that FeRe-based DPs are somewhat different from our CoIr-system. Re^{5+} has two unpaired electrons at $j_{eff} = 3/2$ orbitals whereas for Ir^{4+} these orbitals are complete and there is one unpaired spin at $j_{eff} = 1/2$. Moreover, a quenched orbital moment is expected for Fe^{3+} , whereas Co^{2+} is known to present a non-negligible orbital contribution, as our XMCD results clearly indicate. Our results may find more resemblance with those observed for NiIr-based DPs, since Ni^{2+} may also present orbital contribution to the magnetic moment [51, 52]. For A_2NiIrO_6 ($A = La-Lu$) the systematic in-

crease of T_C and H_C with decreasing A ionic radius is attributed to the increased strength of the AFM $Ni^{2+} e_g - Ir^{4+} t_{2g}$ orbital hybridization [38, 39]. The enhancement of H_C with bending of B–O–B' angle in the $La_{2-x}A_xCoIrO_6$ samples here investigated gives further evidence that the $t_{2g} - O 2p - e_g$ hybridization plays a major role on the CoIr-based DPs.

IV. SUMMARY

In summary, we thoroughly investigated the structural, electronic and magnetic properties of $La_{1.5}Ba_{0.5}CoIrO_6$ (Ba0.5) and $La_{1.5}Ca_{0.5}CoIrO_6$ (Ca0.5) samples by means of XRD, ac and dc magnetization, Co and Ir $L_{2,3}$ -edges and Co K -edge XAS and XMCD. Our results show that the presence of 25% of Ba^{2+}/Ca^{2+} at La^{3+} site leads to Co^{2+}/Co^{3+} mixed valence, while Ir remains mostly in a tetravalent state. For Ca0.5 it is observed a magnetic ordering at ~ 96 K and a large H_C , while for Ba0.5 a magnetic ordering is not clear and the H_C is much smaller. Since both compounds presents nearly the same Co and Ir valence states and effective magnetic moments, the remarkable differences between the magnetic properties of these samples can be understood in terms of changes in the exchange paths between Co e_g/t_{2g} and Ir t_{2g} ($j_{eff} = 1/2$) orbitals. For Ca0.5, the AFM Co $e_g - Ir t_{2g}$ coupling seems to dominate due to its highly distorted structure. For Ba0.5, the increased structural symmetry weakens such hybridization but strengthen the Co $t_{2g} - Ir t_{2g}$ pathway, with the competing interactions leading to a magnetic frustration on this sample. Together with the ASD, the competing magnetic couplings explain the emergence of a SG phase at low temperatures in both compounds.

ACKNOWLEDGMENTS

This work was supported by the Brazilian funding agencies: Fundação Carlos Chagas Filho de Amparo à Pesquisa do Estado do Rio de Janeiro (FAPERJ) [Nos. E-26/202.798/2019 and E-26/211.291/2021], Fundação de Amparo à Pesquisa do Estado de Goiás (FAPEG) and Conselho Nacional de Desenvolvimento Científico e Tecnológico (CNPq) [No. 400633/2016-7]. We thank Diamond Light Source for time on beamline I06 under proposal MM29620-1. We acknowledge DESY (Hamburg, Germany), a member of the Helmholtz Association HGF, for the provision of experimental facilities. Parts of this research were carried out at beamline P09 under proposal I-20200348 and we would like to thank J. Bergtholdt and O. Leupold for assistance in setting up the experiment and 6T/2T/2T vector magnet, respectively.

- [1] K.-I. Kobayashi, T. Kimura, H. Sawada, K. Terakura, and Y. Tokura. Room-temperature magnetoresistance in an oxide material with an ordered double-perovskite structure, *Nature* **395**, 677-680 (1998).
- [2] D. Serrate, J. M. De Teresa, and M. R. Ibarra. Double perovskites with ferromagnetism above room temperature, *J. Phys.: Condens. Matter* **19**, 023201 (2007).
- [3] S. Vasala and M. Karppinen. $A_2B'B''O_6$ perovskites: A review, *Prog. Solid State Chem.* **43**, 1 (2015).
- [4] B. J. Kim, H. Ohsumi, T. Komesu, S. Sakai, T. Morita, H. Takagi, and T. Arima. Phase-Sensitive Observation of a Spin-Orbital Mott State in Sr_2IrO_4 , *Science* **323**, 1329 (2009).
- [5] G. Cao, T. F. Qi, L. Li, J. Terzic, S. J. Yuan, L. E. DeLong, G. Murthy, and R. K. Kaul. Novel Magnetism of Ir^{5+} ($5d^4$) Ions in the Double Perovskite Sr_2YIrO_6 , *Phys. Rev. Lett.* **112**, 056402 (2014).
- [6] B. Raveau and Md. Motin Seikh, *Cobalt Oxides: From Crystal Chemistry to Physics* (Wiley-VCH, Weinheim, 2012).
- [7] J. Song, B. Zhao, L. Yin, Y. Qin, J. Zhou, D. Wang, W. Song, and Y. Sun. Reentrant spin glass behavior and magnetodielectric coupling of an Ir-based double perovskite compound, La_2CoIrO_6 , *Dalton Trans.* **46**, 11691 (2017).
- [8] S. Lee, M. C. Lee, Y. Ishikawa, P. Miao, S. Torii, C. J. Won, K. D. Lee, N. Hur, D. Y. Cho, and T. Kamiyama. Magnetoelastic octahedral breathing mode in the ferromagnetic La_2CoIrO_6 double perovskite, *Phys. Rev. B* **98**, 104409 (2018).
- [9] N. Narayanan, D. Mikhailova, A. Senyshyn, D. M. Trots, R. Laskowski, P. Blaha, K. Schwarz, H. Fuess, and H. Ehrenberg. Temperature and composition dependence of crystal structures and magnetic and electronic properties of the double perovskites $La_{2-x}Sr_xCoIrO_6$ ($0 \leq x \leq 2$), *Phys. Rev. B* **82**, 024403 (2010).
- [10] M.-C. Lee, C. H. Sohn, S. Y. Kim, K. D. Lee, C. J. Won, N. Hur, J.-Y. Kim, D.-Y. Cho, and T. W. Noh. Stabilization of ferromagnetic ordering in cobaltite double perovskites of La_2CoIrO_6 and La_2CoPtO_6 , *J. Phys.: Condens. Matter* **27**, 336002 (2015).
- [11] L. Buřaıçal, E. Sadrollahi, F. J. Litterst, D. Rigitano, E. Granado, L. T. Coutrim, E. B. Araújo, M. B. Fontes, E. Baggio-Saitovitch, and E. M. Bittar. Effect of structural and magnetic disorder on the $3d-5d$ exchange interactions in $La_{2-x}Ca_xCoIrO_6$, *Phys. Rev. B* **102** (2020) 024436.
- [12] M.-C. Lee, S. Lee, C. J. Won, K. D. Lee, N. Hur, J. L. Chen, D. Y. Cho, and T. W. Noh. Hybridized orbital states in spin-orbit coupled $3d-5d$ double perovskites studied by x-ray absorption spectroscopy, *Phys. Rev. B* **97**, 125123 (2018).
- [13] W. Jin, S. H. Chun, J. Kim, D. Casa, J. P. C. Ruff, C. J. Won, K. D. Lee, N. Hur, and Y.-J. Kim. Magnetic excitations in the double-perovskite iridates $La_2M'IrO_6$ ($M = Co, Ni, \text{ and } Zn$) mediated by $3d-5d$ hybridization, *Phys. Rev. B* **105**, 054419 (2022).
- [14] D. Takegami, D. Kasinathan, K. K. Wolff, S. G. Altdorf, C. F. Chang, K. Hofer, A. Melendez-Sans, Y. Utsumi, F. Meneghin, T. D. Ha, C. H. Yen, K. Chen, C. Y. Kuo, Y. F. Liao, K. D. Tsuei, R. Morrow, S. Wurmehl, B. Büchner, B. E. Prasad, M. Jansen, A. C. Komarek, P. Hansmann, and L. H. Tjeng. Charge-transfer energy in iridates: A hard x-ray photoelectron spectroscopy study, *Phys. Rev. B* **102**, 045119 (2020).
- [15] A. Kolchinskaya, P. Komissinskiy, M. B. Yazdi, M. Vafae, D. Mikhailova, N. Narayanan, H. Ehrenberg, F. Wilhelm, A. Rogalev, and L. Alf. Magnetism and spin-orbit coupling in Ir-based double perovskites $La_{2-x}Sr_xCoIrO_6$, *Phys. Rev. B* **85**, 224422 (2012).
- [16] L. T. Coutrim, E. M. Bittar, F. Stavale, F. Garcia, E. Baggio-Saitovitch, M. Abbate, R. J. O. Mossaneck, H. P. Martins, D. Tobia, P. G. Pagliuso, and L. Buřaıçal. Compensation temperatures and exchange bias in $La_{1.5}Ca_{0.5}CoIrO_6$, *Phys. Rev. B* **93**, 174406 (2016).
- [17] L. T. Coutrim, E. M. Bittar, F. Garcia, and L. Buřaıçal. Influence of spin glass-like magnetic relaxation on the zero-field-cooled exchange bias effect, *Phys. Rev. B* **98** (2018) 064426.
- [18] L. Buřaıçal, L. T. Coutrim, E. M. Bittar, and F. Garcia. A phenomenological model for the spontaneous exchange bias effect, *J. Magn. Magn. Mater.* **512** (2020) 167048.
- [19] L. T. Coutrim, E. M. Bittar, E. Baggio-Saitovitch, and L. Buřaıçal. Spin glass-like properties and exchange bias in $La_{1.5}Sr_{0.5}CoIrO_6$, *J. Magn. Magn. Mater.* **441**, 243 (2017).
- [20] A. C. Larson and R. B. Von Dreele. General structure analysis system - GSAS/EXPGUI, Los Alamos National Laboratory Report No. LAUR 86-748, 2000; B. H. Toby. *EXPGUI*, a graphical user interface for *GSAS*, *J. Appl. Crystallogr.* **34**, 210 (2001).
- [21] J. Strempler, S. Francoual, D. Reuther, D. K. Shukla, A. Skaugen, H. Schulte-Schrepping, T. Kracht and H. Franz. Resonant scattering and diffraction beamline P09 at PETRA III, *J. Synchrotron Rad.* **20**, 541 (2013).
- [22] J. Strempler, J. R. L. Mardegan, S. Francoual, L. Veiga, L. Bouchenoire, T. Spitzbart and H. Zink. Fast helicity switching of x-ray circular polarization at beamline P09 at PETRA III, *AIP conference proceedings* **1741**, 030017 (2016).
- [23] P. D. Battle, J. G. Gore, R. C. Hollyman, A. V. Powell. The magnetic properties of $BaLaCoIrO_6$ and $Ba_3CoIr_xRu_{2-x}O_9$, *J. Alloy. Compd.* **218**, 110-116 (1995).
- [24] C. J. Howard, B. J. Kennedy and P. M. Woodward. Ordered double perovskites - a group-theoretical analysis, *Acta Cryst.* **B59**, 463-471 (2003).
- [25] R. D. Shannon. Revised effective ionic radii and systematic studies of interatomic distances in halides and chalcogenides, *Acta Cryst.* **A32**, 751 (1976).
- [26] P. Woodward, R.-D. Hoffmann, and A. W. Sleight. Order-disorder in $A_2M^{3+}M^{5+}O_6$ perovskites, *J. Mater. Res.* **9**, 8 (1994).
- [27] A. F. J. Morgownik and J. A. Mydosh. High-temperature susceptibility of the CuMn spin-glass, *Phys. Rev. B* **24**, 5277 (1981).
- [28] J. A. Mydosh. Spin glasses: redux: an updated experimental/materials survey, *Rep. Prog. Phys.* **78**, 052501 (2015).
- [29] J. Souletie and J. L. Tholence. Critical slowing down in spin glasses and other glasses: Fulcher versus power law, *Phys. Rev. B* **32**, 516 (1985).

- [30] J. A. Mydosh, *Spin Glasses: An Experimental Introduction* (Taylor & Francis, London, 1993).
- [31] A. Malinowski, V. L. Bezusyy, R. Minikayev, P. Dziawa, Y. Syryanyy, and M. Sawicki. Spin-glass behavior in Ni-doped $\text{La}_{1.85}\text{Sr}_{0.15}\text{CuO}_4$, *Phys. Rev. B* **84**, 024409 (2011).
- [32] V. K. Anand, D. T. Adroja, and A. D. Hillier. Ferromagnetic cluster spin-glass behavior in PrRhSn_3 , *Phys. Rev. B* **85**, 014418 (2012).
- [33] T. Dey, A. Maljuk, D. V. Efremov, O. Kataeva, S. Gass, C. G. F. Blum, F. Steckel, D. Gruner, T. Ritschel, A. U. B. Wolter, J. Geck, C. Hess, K. Koepf, J. van den Brink, S. Wurmehl, and B. Büchner. Ba_2YrO_6 : A cubic double perovskite material with Ir^{5+} ions, *Phys. Rev. B* **93**, 014434 (2016).
- [34] S. Agrestini, K. Chen, C.-Y. Kuo, L. Zhao, H.-J. Lin, C.-T. Chen, A. Rogalev, P. Ohresser, T.-S. Chan, S.-C. Weng, G. Auffermann, A. Völzke, A. C. Komarek, K. Yamaura, M. W. Haverkort, Z. Hu, and L. H. Tjeng. Nature of the magnetism of iridium in the double perovskite $\text{Sr}_2\text{CoIrO}_6$ *Phys. Rev. B* **100**, 014443 (2019).
- [35] K. K. Wolff, L. H. Tjeng, and M. Jansen. The new ordered double perovskite SrLaCuIrO_6 , *Solid State Commun.* **289**, 43-46 (2018).
- [36] M. Sikora, Cz. Kapusta, M. Borowiec, C. J. Oates, V. Prochazka, D. Rybicki, D. Zajac, J. M De Teresa, C. Marquina, and M. R Ibarra. Evidence of unquenched Re orbital magnetic moment in $AA'\text{FeReO}_6$ double perovskites, *Appl. Phys. Lett.* **89**, 062509 (2006).
- [37] C. A. Escanhoela, G. Fabbris, F. Sun, C. Park, J. Gopalakrishnan, K. Ramesha, E. Granado, N. M. Souza-Neto, M. van Veenendaal, and D. Haskel. Tuning magnetic coercivity with external pressure in iron-rhenium based ferrimagnetic double perovskites, *Phys. Rev. B* **98**, 054402 (2018).
- [38] Timothy Ferreira, Gregory Morrison, Jeongho Yeon, and Hans-Conrad zur Loye. Design and Crystal Growth of Magnetic Double Perovskite Iridates: $\text{Ln}_2\text{MIR}_2\text{O}_6$ ($\text{Ln} = \text{La, Pr, Nd, Sm-Gd}$; $\text{M} = \text{Mg, Ni}$), *Cryst. Growth Des.* **16**, 5 (2016).
- [39] Hai L. Feng, Zheng Deng, Meixia Wu, Mark Croft, Saul H. Lapidus, Sizhan Liu, Trevor A. Tyson, Bruce D. Ravel, Nicholas F. Quackenbush, Corey E. Frank, Changqing Jin, Man-Rong Li, David Walker, and Martha Greenblatt. High-Pressure Synthesis of $\text{Lu}_2\text{NiIrO}_6$ with Ferrimagnetism and Large Coercivity, *Inorg. Chem.* **58**, 1 (2019).
- [40] D. K. Bora, X. Cheng, M. Kapilashrami, P. A. Glans, Y. Luo and J.-H. Guo. Influence of crystal structure, ligand environment and morphology on Co L -edge XAS spectral characteristics in cobalt compounds, *J. Synchrotron Rad.* **22**, 1450-1458 (2015).
- [41] B. T. Thole, P. Carra, F. Sette, and G. van der Laan. X-Ray Circular Dichroism as a Probe of Orbital Magnetization, *Phys. Rev. Lett.* **68**, 1943 (1992).
- [42] P. Carra, B. T. Thole, M. Altarelli, and X. Wang. X-Ray Circular Dichroism and Local Magnetic Fields, *Phys. Rev. Lett.* **70**, 694 (1993).
- [43] Y. Teramura, A. Tanaka, and T. Jo. Effect of Coulomb Interaction on the X-Ray Magnetic Circular Dichroism Spin Sum Rule in $3d$ Transition Elements, *J. Phys. Soc. Jpn.* **65**, 1053 (1996).
- [44] C. Piamonteze, P. Miedema, and F. M. F. de Groot. Accuracy of the spin sum rule in XMCD for the transition-metal L edges from manganese to copper, *Phys. Rev. B* **80**, 184410 (2009).
- [45] X. Liu, M. Kotiuga, H. Kim, A. T. N'Diaye, Y. Choi, Q. Zhang, Y. Cao, M. Kareev, F. Wen, B. Pal, J. W. Freeland, L. Gu, D. Haskel, P. Shafer, E. Arenholz, K. Haule, D. Vanderbilt, K. M. Rabe, and J. Chakhalian. Interfacial charge-transfer Mott state in iridate/nickelate superlattices, *P. Natl. Acad. Sci. USA* **116**, 19863-19868 (2019).
- [46] D. Yi, J. Liu, S.-L. Hsu, L. Zhang, Y. Choi, J.-W. Kim, Z. Chen, J. D. Clarkson, C. R. Serrao, E. Arenholz, P. J. Ryan, H. Xu, R. J. Birgeneau, and . Ramesh. Atomic-scale control of magnetic anisotropy via novel spin-orbit coupling effect in $\text{La}_{2/3}\text{Sr}_{1/3}\text{MnO}_3/\text{SrIrO}_3$ superlattices, *P. Natl. Acad. Sci. USA* **113**, 23 (2016).
- [47] S. Fujiyama, H. Ohsumi, K. Ohashi, D. Hirai, B. J. Kim, T. Arima, M. Takata, and H. Takagi. Spin and Orbital Contributions to Magnetically Ordered Moments in $5d$ Layered Perovskite Sr_2IrO_4 , *Phys. Rev. Lett.* **112**, 016405 (2014).
- [48] G. Jackeli and G. Khaliullin. Mott Insulators in the Strong Spin-Orbit Coupling Limit: From Heisenberg to a Quantum Compass and Kitaev Models, *Phys. Rev. Lett.* **102**, 017205 (2009).
- [49] S. Ganguly, S. Bhowal. Study of nontrivial magnetism in $3d$ - $5d$ transition metal based double perovskites, *Phys. Rev. B* **101**, 085104 (2020).
- [50] R. Morrow, K. Samanta, T. S. Dasgupta, J. Xiong, J. W. Freeland, D. Haskel, and P. M. Woodward. Magnetism in $\text{Ca}_2\text{CoOsO}_6$ and $\text{Ca}_2\text{NiOsO}_6$: Unraveling the Mystery of Superexchange Interactions between $3d$ and $5d$ Ions, *Chem. Mater.* **28**, 3666-3675 (2016).
- [51] V. Fernandez, C. Vettier, F. de Bergevin, C. Giles, and W. Neubeck. Observation of orbital moment in NiO, *Phys. Rev. B* **57**, 7870 (1998).
- [52] S. K. Kwon and B. I. Min. Unquenched large orbital magnetic moment in NiO, *Phys. Rev. B* **62**, 73 (2000).